SUPPLEMENTAL MATERIAL

for

Exceptionally Low Shear Modulus in a Prototypical Imidazole-Based Metal-Organic Framework

Jin-Chong Tan,[1] Bartolomeo Civalleri,[2] Chung-Cherng Lin,[3] Loredana Valenzano,[2,4] Raimondas Galvelis,[5] Po-Fei Chen,[6] Thomas D. Bennett,[1] Caroline Mellot-Draznieks,[5,7] Claudio M. Zicovich-Wilson[8] & Anthony K. Cheetham[1*]

[1]Department of Materials Science and Metallurgy, University of Cambridge, Pembroke St., Cambridge CB2 3QZ, U.K.
[2]Department of Inorganic, Physical and Materials Chemistry, NIS Centre of Excellence, and INSTM Reference Center, University of Turin, via P. Giuria 7, 10125 Torino, Italy.
[3]Institute of Earth Sciences, Academia Sinica, Nankang, Taipei, Taiwan 115, R.O.C.
[4]Department of Physics, Michigan Technological University, 1400 Townsend Drive, Houghton, MI 49931-1295, U.S.A.
[5]Department of Chemistry, University College London, 20 Gordon St., London, WCH1 0AJ, U.K.
[6]Department of Earth Sciences and Graduate Institute of Geophysics, National Central University, Jhongli, Taiwan 32001, R.O.C.
[7]Laboratoire de Chimie et Biologie des Métaux, Université Joseph Fourier, Grenoble, CNRS, UMR 5249, CEA, DSV/iRTSV, 17 rue des Martyrs, F-38054, Grenoble cedex 9, France.
[8]Facultad de Ciencias, Universidad Autonoma del Estado de Morelos, Av. Universidad 1001, 62209 Cuernavaca, Mexico.

*Correspondence can be addressed to either: J.C.T. (jct33@cam.ac.uk), B.C. (bartolomeo.civalleri@unito.it) or A.K.C. (akc30@cam.ac.uk).

Table of Contents

1 Materials Synthesis and Characterization

ZIF-8 were synthesized *via* solvothermal reactions according to procedures reported in ref. [1]. The products consisted of truncated rhombic-dodecahedral single crystals up to 300 μm across, confirmed to be ZIF-8 by X-ray diffraction (Fig.S1). The use of DMF (*N*, *N*-dimethylformamide) in synthesis yielded crystals with solvent molecules trapped within the framework pore structures. It was therefore imperative to optimally evacuate the as-synthesized crystals intended for Brillouin scattering experiments (§2) and nanoindentation studies (§5). To avoid damaging the single crystals, the DMF molecules were removed by solvent-exchange in methanol overnight, followed by evacuation for 24 hours at room temperature, then at 150 ºC for 6 hours. FTIR spectroscopy (Fig.S2) and thermogravimetric analyses (Fig.S3) confirmed that the pores of the evacuated crystals were indeed free of DMF. The permanent porosity characteristic of the ZIF-8 structure was further confirmed *via* X-ray diffraction. Fig.S1 shows that the solvent-free ZIF-8 is highly crystalline, confirming that the structural integrity of the framework is unaffected by the evacuation process being adopted here.

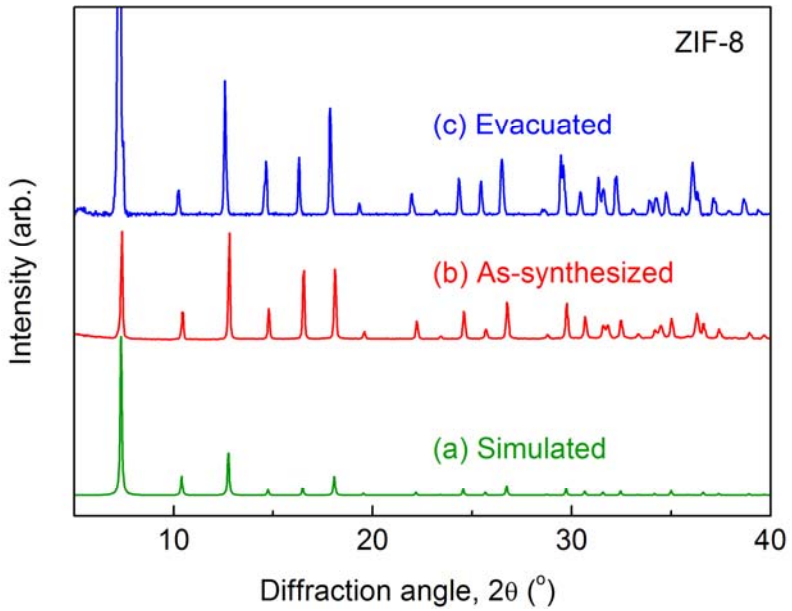

Fig.S1. Powder X-ray diffraction of ZIF-8: (a) simulated pattern, (b) as-synthesized structure in which the SOD cages contain both water and DMF molecules, and (c) after desolvation and evacuation.

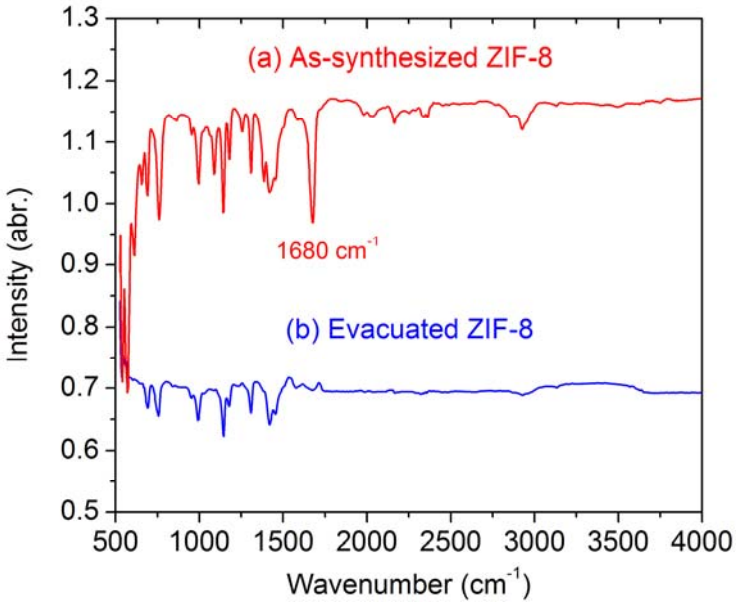

Fig.S2. FTIR spectra of (a) as-synthesized ZIF-8 with DMF in the pores, and (b) desolvated crystals that are free of DMF, evidenced by the loss of the carbonyl peak at about 1680 cm^{-1}.

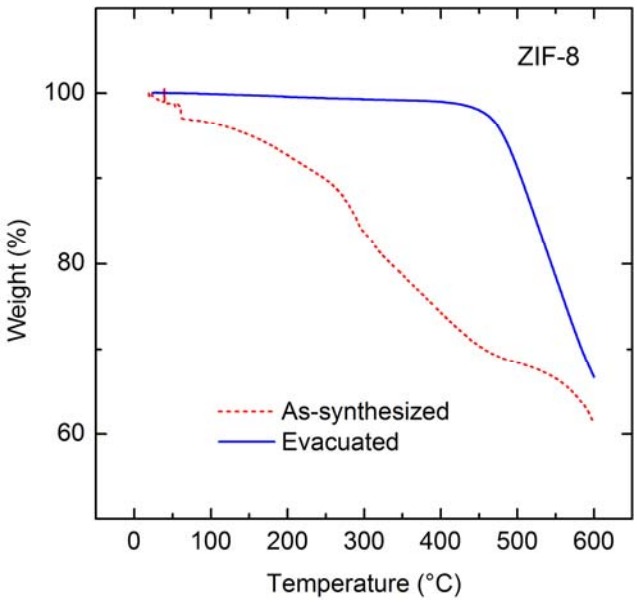

Fig.S3. Thermogravimetric curves of the as-synthesized and evacuated ZIF-8 bulk samples. The as-synthesized framework structure loses water and DMF molecules continuously upon heating, whereas the evacuated structure exhibits negligible weight loss up to around 450°C, beyond which thermal decomposition sets in.

2 Brillouin Scattering Experiments

Brillouin spectroscopy was performed under ambient conditions (21.5 ± 0.5 ºC, 1 atm) using an argon ion laser ($\lambda = 514.5$ nm) as excitation source. The scattered light was analyzed using a six-pass tandem Fabry-Pérot interferometer (JRS Scientific Instruments) and the spectrum recorded by a photomultiplier detector. The transparent, solvent-free single crystals of ZIF-8 (~150 μm in size) were carefully ground and polished to a thickness of 20 – 25 μm. Opposite faces of the polished plates were parallel to each other to within 1º. The specimen thus prepared was secured in a pair of cover glasses for optical alignment. To ensure better data reliability, two specimens were measured (Fig.S4).

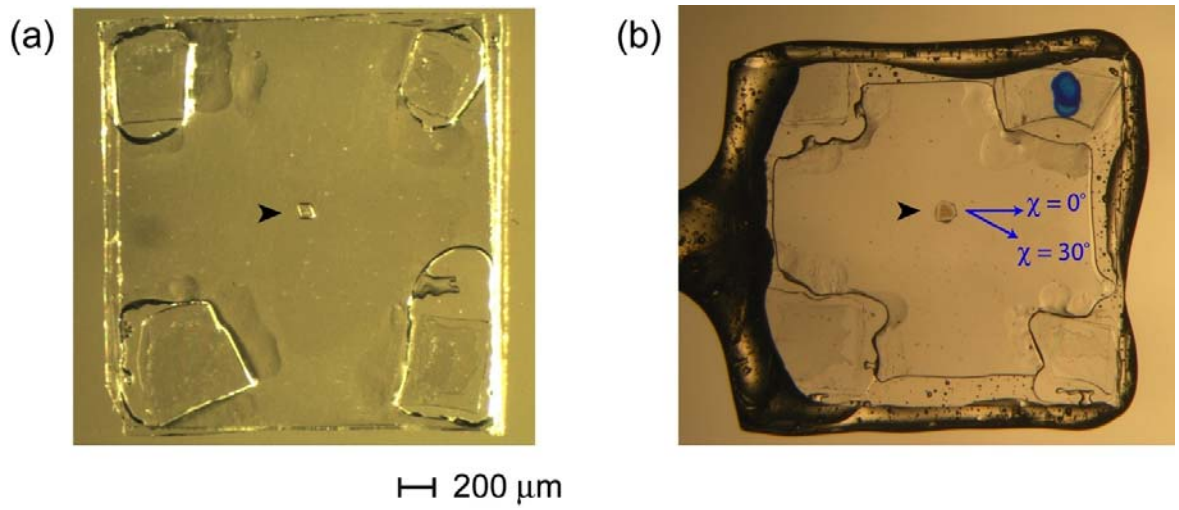

Fig.S4. Solvent-free single crystals of ZIF-8 for Brillouin scattering: (a) Specimen A, and (b) Specimen B. Note that the crystal is located approximately in the middle of the image, sandwiched between a pair of protective glass cover slips (thickness ~100 μm). The lateral dimensions of the polished ZIF-8 platelets are ~150 μm across, and each has a thickness of ~25 μm. *N.B.* Our initial studies using as-synthesized crystals were unsuccessful; the solvent-containing ZIF-8 did not show any recognizable Brillouin signal due to the intense background produced by disordered DMF.

A 45º/45º symmetric scattering geometry was adopted in our experiment with which the acoustic velocity (*V*) is given by [2]: $V = \lambda\Delta\omega/\sqrt{2}$, where $\Delta\omega$ is the Brillouin shift, and λ is the wavelength of the incident laser. Importantly, a relatively low power of 20 to 25 mW

was adopted during measurements to prevent sample degradation by laser irradiation (this was confirmed by single-crystal X-ray diffraction); data collection for each spectrum took between 40 to 80 minutes depending on orientation of the phonon involved. The acoustic velocities at each χ-angle used in the calculation were the averages of 2 ~ 3 spectra. It is noted that the χ-angle is defined in relation to an arbitrary setting mark on the three-circle Eulerian cradle to which the specimen was mounted, see Fig.S4b. Because of the 45º/45º symmetric scattering geometry adopted here, it was only necessary to collect the Brillouin spectra over the range $0º \leq \chi \leq 180º$ (in intervals of 10º or 15º). The acoustic velocity data of specimens A and B are listed in Tables S1 & S2, respectively. To ensure better data reliability, the velocities determined from both specimens were combined to solve for the single-crystal elastic constants C_{ij}s (Table S3).

Table S1. Acoustic velocities (V) determined from the Brillouin shifts ($\Delta\omega$) of Specimen A. The velocity of the longitudinal wave (L), and the fast and slow transverse waves (T_F & T_S) are tabulated as a function of the χ-angle.

ZIF-8: Specimen A		Temperature = 21.7 ± 0.2 ºC Acoustic velocities in m/sec				
χ (º)	**Waves**	**1) Area-1**	**2) Area-1**	**3) Area-2**	**4) Area-2**	**Average**
0	L	3162		3182	—	**3172**
	T_F	1276		1180	1205	**1234**
	T_S	1040		1034	1031	**1036**
15	L	3151		3121		**3136**
	T_F	1299		1221		**1260**
	T_S	1065		1045		**1055**
30	L	3140		3121		**3131**
	T_F	1307		1215		**1261**
	T_S	1067		1047		**1057**
45	L	3167		3144		**3156**
	T_F	1278		1160		**1219**
	T_S	1038		1033		**1036**
60	L	3173		3138		**3156**
	T_F	1162		1096		**1129**
	T_S	1007		993		**1000**
75	L	3137		3110		**3124**
	T_F	1005		986		**996**
	T_S	1005		986		**996**
90	L	3060	—	3140		**3100**
	T_F	1212	1220	1199		**1208**
	T_S	1016	1013	1012		**1013**
105	L	3144	—	3105	3103	**3124**
	T_F	1221	1216	1186	1191	**1204**
	T_S	1048	1049	1035	1036	**1042**
120	L	3067	3080	3111		**3092**
	T_F	1264	1236	1161		**1206**
	T_S	1051	1048	1040		**1045**
135	L	3110		3123		**3117**
	T_F	1196		1136		**1166**

	T_S	1036		1023		**1030**
150	L	3088		3120		**3104**
	T_F	1104		1077		**1091**
	T_S	998		992		**995**
165	L	3130		3124		**3127**
	T_F	1261		1243		**1252**
	T_S	1001		1003		**1002**
180	L	3063		3150		**3107**
	T_F	1155		1259		**1207**
	T_S	1017		1047		**1032**

Table S2. Acoustic velocity data of Specimen B.

ZIF-8: Specimen B		Temperature = 21.7 ± 0.2 ºC Acoustic velocities in m/sec				
χ (º)	**Waves**	**1) Area-1**	**2) Area-1**	**3) Area-2**	**4) Area-2**	**Average**
0	L	3061	3124	—	—	**3093**
	T_F	1049	1045	1074	1065	**1058**
	T_S	1049	1045	1074	1065	**1058**
10	L	3053	3115	3125	3119	**3084**
	T_F	1245	1211			**1228**
	T_S	1037	1026			**1032**
20	L	3096	3119			**3108**
	T_F	---	1140			**1140**
	T_S	1029	1020			**1025**
30	L	3116	3136			**3126**
	T_F	1159	1153			**1156**
	T_S	1027	1023			**1025**
40	L	3105	3128			**3117**
	T_F	1153	1172			**1163**
	T_S	1041	1040			**1041**
50	L	3111	3112			**3112**
	T_F	1238	1231			**1235**
	T_S	1055	1056			**1056**
60	L	3041	3107			**3074**
	T_F	1179	1241			**1210**
	T_S	1057	1056			**1057**
70	L	3083	3102			**3093**
	T_F	1156	1154			**1155**
	T_S	1050	1051			**1051**
80	L	3109	3157			**3109**
	T_F	1183	1166			**1175**
	T_S	1058	1043			**1051**
90	L	3111	3113			**3112**
	T_F	1185	1164			**1175**
	T_S	1050	1034			**1042**
	L	3031	3131			**3081**

100	T_F	1174	1149			**1162**
	T_S	1050	1034			**1042**
110	L	3052	3136			**3094**
	T_F	1332	1256			**1294**
	T_S	1054	1042			**1048**
120	L	3068	3143			**3106**
	T_F	1084	1079			**1082**
	T_S	1015	996			**1006**
130	L	3085	3072	3087		**3081**
	T_F	1059	1077	1072		**1069**
	T_S	1001	1012	1012		**1008**
140	L	3063	3110			**3087**
	T_F	1153	1128			**1141**
	T_S	1034	1027			**1031**
150	L	3078	3086			**3082**
	T_F	1076	1061			**1069**
	T_S	1005	1008			**1007**
160	L	2997	3067	3066		**3067**
	T_F	1116	1132	1116		**1121**
	T_S	1033	1036	1035		**1035**
170	L	3097	3085			**3091**
	T_F	1095	1071			**1083**
	T_S	1024	1000			**1012**
180	L	3035	3075	3055		**3075**
	T_F	1065	1048	1039		**1051**
	T_S	1065	1048	1039		**1051**

Data were not included in averaging
Data collected at the same position, hence not included in averaging
Data were not adopted for solving the C_{ij}s for a number of combinations shown in Table S3

Table S3. Single-crystal elastic constants C_{ij}s of ZIF-8, based on the combination of the acoustic velocity data of specimens A and B (Tables S1 & S2). For each set of velocity combination, linearized least-squares inversion [3] was performed until global convergence of solutions was obtained. This procedure has been previously applied successfully for finding solutions to the Christoffel's matrix (*e.g.* [4]). Here we demonstrate that the resulting values of C_{ij}s are not sensitive towards the different combinations tested here. Furthermore, we obtained a very similar set of results by applying a genetic algorithm method [5]: C_{11} = 9.5506 GPa, C_{12} = 6.8088 GPa and C_{44} = 0.9626 GPa, thereby confirming the validity of our former approach. All calculations were performed by taking the density of ZIF-8 as 0.95 g/cm^3, which corresponds to the crystallographic density of the solvent-free framework determined by single-crystal X-ray diffraction.

Combination	Elastic constants, C_{ij}s (GPa)		
	C_{11}	C_{12}	C_{44}
1a	9.5191	6.8566	0.9715
1b/1c	9.5115	6.8483	0.9712
1d	9.5318	6.8562	0.9692
1e	9.5248	6.8478	0.9687
2a	9.5289	6.8822	0.9604
2b/2c	9.5204	6.8730	0.9601
2d	9.5262	6.8821	0.9662
2e	9.5180	6.8732	0.9660
Average:	**9.5226**	**6.8649**	**0.9667**
Standard deviation, 1σ:	**0.0066**	**0.0144**	**0.0044**

Note:

The combinations are based on a consideration of different velocity sets, denoted as "**nm**" (**n** = **1**,**2**; **m** = **a**,**b**,**c**,**d**,**e**), of which cases **1** and **2** correspond to Specimen B while cases **a**–**e** designate Specimen A. The treatment was as follows:

- For Specimen B (Table S2):
  Case **1**: Based on all velocity data.

Case **2**: The data collected at χ = 10º, 50º, and 110º were omitted from the calculation. These data points can be considered as outliers since the quality of the T_F signal in Specimen B appears to be less reliable than those measured in Specimen A.

- For Specimen A (Table S1):

  Case **a**: Omit data at χ = 165º, consider *L* at $\chi = 180º$ (3150 m/sec)

  Case **b**: Omit data at $\chi = 165º$, consider *L* at $\chi = 180º$ (3107 m/sec)

  Case **c**: Omit data at χ = 165º, consider *L* at $\chi = 180º$ (3107 m/sec); but the initial C_{ij}s are C_{11} = 8.83, C_{12} = 7.03 and C_{44} = 1.40 GPa

  Case **d**: Include data at χ = 165º, *L* at $\chi = 180º$ (3150 m/sec)

  Case **e**: Include data at χ = 165º, *L* at $\chi = 180º$ (3107 m/sec)

- The fitted normal vectors of specimens A and B are (–0.480, –0.650, –0.590) and (0.403, 0.624, –0.675) respectively, and the rms deviation between the calculated and measured velocities are 45 m s^{-1} and 27 m s^{-1}, respectively (applicable to the data presented in Figs.1(c) and 1(d) in the Manuscript).

3 *Ab Initio* Quantum Mechanical Calculations

Ab initio predictions of the elastic constants (C_{ij}s) were carried out using the periodic CRYSTAL09 code [6] based on the atom-centered (Gaussian-type) basis set. We adopted the hybrid B3LYP level of theory, by virtue of its high-quality predictions on the structure and properties of a wide range of crystalline systems, including those of MOF-5 [7]. First, we performed a full relaxation of the ZIF-8 structure (cell parameters and atomic positions) at which the crystal symmetry was maintained during the optimization procedure. At equilibrium, the cell parameter was found to be a = 17.3481 Å, indicating an overestimation of ~2% compared with the experimental value (see Table S4). Using the optimized structure as the starting geometry, the full elastic tensor was computed according to the algorithm described in ref.[8], to which the ZIF-8 structure was subjected to a finite adimensional deformation of $\pm$0.005 (*i.e.* either normal strain ε or shear strain γ). Furthermore, we have compared the numerical accuracy of the different Hamiltonians for predicting the C_{ij}s, and to evaluate the performance of basis sets of different sizes (Table S4). The theoretical calculations were also used to elucidate the underlying elastic deformation mechanisms surrounding ZIF-8.

Table S4. Single-crystal elastic constants (C_{ij}s) and bulk modulus (K) of ZIF-8, calculated using the density-functional theory (DFT) and the Hartree-Fock (HF) methods. For the DFT methods, we implemented the B3LYP [9] hybrid functional and the gradient-corrected PBE [10] functional. In addition, simulations were performed using functionals augmented with an empirical dispersion term, such as the B3LYP-D* [11] and PBE-D [12]. All theoretical results correspond to 0 K. Results highlighted in blue are predictions that appear to be consistent with experiments (295 K, see Table S3); red denotes *spurious* predictions due to basis set superposition error (BSSE), of which C_{11}<C_{12} implies one of the fundamental elastic stability criteria has been violated; pink designates predicted C_{44} with a deviation of >50% compared to the measured value of 0.97 GPa.

ZIF-8	*Basis set*	*NP (Step)*[a]	*a* (Å)[b]	C_{11}	C_{12} (GPa)	C_{44}	K[c] (GPa)
B3LYP[d]	BS2	3 (0.005)	17.3481	11.04	8.33	0.94	9.23 (9.04)
B3LYP-D*	BS2	3 (0.005)	17.0630	11.03	8.43	0.73	9.30
PBE	BS1	3 (0.005)	17.1907	6.38	10.02	0.94	8.8 (8.7)
	BS1	5 (0.005)	17.1907	9.72	11.05	1.50	10.6 (8.7)
	BS2	3 (0.005)	17.2606	10.14	8.00	0.78	8.7 (8.5)
PBE-D	BS1	3 (0.005)	16.8640	4.98	7.92	0.33	6.9 (8.2)
	BS2	3 (0.005)	16.9264	9.79	7.03	0.53	7.95 (8.00)
	BS3	3 (0.005)	16.9672	9.62	6.53	0.46	7.56
HF[e]	BS2	3 (0.005)	17.4548	12.36	9.36	1.40	10.36
	BS2	5 (0.005)	17.4548	13.47	9.30	1.42	10.69
	BS2	7 (0.005)	17.4548	10.17	9.29	1.36	9.59

- Three basis sets were considered in this study, increasing in size from BS1 to BS3:
  BS1: Zn[8-64111-41G(f)], C/N/H[6-31G(d,p)]
  BS2: Zn[8-64111-41G(f)], C/N/H[6-311G(d,p)]
  BS3: Zn[modified TZVP], C/N/H[TZP]

[a] Number of points (step size) for numerical differentiation of the analytic cell gradients [8]. They either correspond to the normal (ε = cubic to tetragonal deformation) or shear (γ = cubic to monoclinic distortion) mechanical deformations applied onto the framework structure to induce small elastic strains of ±0.5% (apart from HF BS2 with applied strains of up to ±1.5%), from which the stress tensor (σ_{ij}) was calculated.

[b] Experimental cell parameter of ZIF-8 determined by (i) single-crystal X-ray diffraction [13]: a = 16.9920(8) Å at 293 K, (ii) neutron powder diffraction [14]: 16.9900(2) Å at 3.5 K and 17.0117(4) at 200 K.

[c] Bulk modulus derived from the C_{ij} elastic tensor, *i.e.* $K = (C_{11} + 2C_{12})/3$ (ref.[15]). For comparison, expressed in brackets are the K values estimated based on the 3rd order Birch-Murnaghan equation-of-state (fitting of 7-point energy-volume curve, $E(V)$, in the range $0.98V_0 < V < 1.02V_0$).

[d] An example input file for B3LYP (BS2) is given in §9.

[e] Calculations at the Hartree-Fock (HF) level of theory could avoid complications associated with the numerical integration grids, but the predicted C_{ij}s tend to be relatively higher due to the neglect of correlation energy.

3.1 On the Role of Methyl Groups

To understand the contribution of methyl groups (CH_3) towards the elasticity of ZIF-8, we have constructed a hypothetical ZIF structure, ZIF-8-H (Table S5), which retains the same atomic positions as in sodalite ZIF-8, but with all the CH_3 groups being replaced by hydrogen. Notably, both the C_{11} and C_{12} stiffness coefficients of the hypothetical structure were found to be appreciably more compliant than those of ZIF-8 (*i.e.* 7.04 GPa *vs*. 11.04 GPa for C_{11}; 5.58 GPa *vs*. 8.33 GPa for C_{12}), while the relatively small variation in the shear coefficient C_{44} indicates that shear deformation is only marginally affected. Indeed, our calculations highlight that bulky substituents in ZIFs have the propensity to make the potential energy surfaces (PES) more *rigid*, conferring greater stiffnesses as their associated steric effects further enhance repulsion when subjected to normal stresses.

Table S5. ZIF-8-H is a hypothetical structure of ZIF-8, for which each of the CH_3 group in the original framework has been replaced by a hydrogen atom.

ZIF-8-H	*Basis set*	*NP (Step)*	*a* (Å)	C_{11}	C_{12}	C_{44}	K
B3LYP	BS2	3 (0.005)	17.1652	7.04	5.58	1.16	6.07

3.2 On the Role of Chemical Bonds on Framework Flexibility

To elucidate the mechanisms surrounding the elastic deformation of ZIF-8, we study the changes in bond lengths and bond angles as a function of externally applied strains. Here we consider a set of calculations performed at the Hartree-Fock (HF) level of theory (Table S4), for which the C_{ij}s were computed by imposing elastic strains of $\pm$1.5%; similar trends were obtained from the B3LYP level of theory.

Our *ab initio* calculations reveal that the ZIF-8 framework deforms through a combination of: (i) Zn–N bonds stretching/compression (Fig.S5), and (ii) tetrahedral N–Zn–N and bridging Zn–mIm–Zn bonds bending (Fig.S7). While the ZnN_4 tetrahedra of ZIF-8 appears to be *soft* and flexible in nature, we found that the imidazolate rings remain *rigid* throughout elastic deformation and, the changes of other bond lengths and angles are also inconsequential.

As shown in Fig.S5(a), significant changes in the Zn–N bond lengths occur when the ZIF-8 framework is subjected to a uniaxial (normal) deformation, from which a total variation of up to ~0.8% was predicted in response to a total external strain of 3%. Specifically, the Zn–N bonds extend in unison when a uniaxial tensile strain is applied (ε positive), and they contract under a compressive strain (ε negative). In contrast, changes to the Zn–N bond lengths are appreciably lower with respect to shear deformation (*i.e.* cubic-to-monoclinic distortion) (Fig.S5(b)), to which the maximum variation is predicted to be just ~0.12%. Thus it is clear that changes in bond lengths play only a minor role in facilitating shear deformation. We also note that because of the anti-parallel nature of shear loading, a bond extension will be accompanied by another bond undergoing contraction, both of which are of a similar magnitude but acting in opposite directions (of course, such bonds are related *via* a mirror plane with respect to an externally applied load, *e.g.* Zn1–N1 *vs.* Zn1–N2 in Fig.S5(b)).

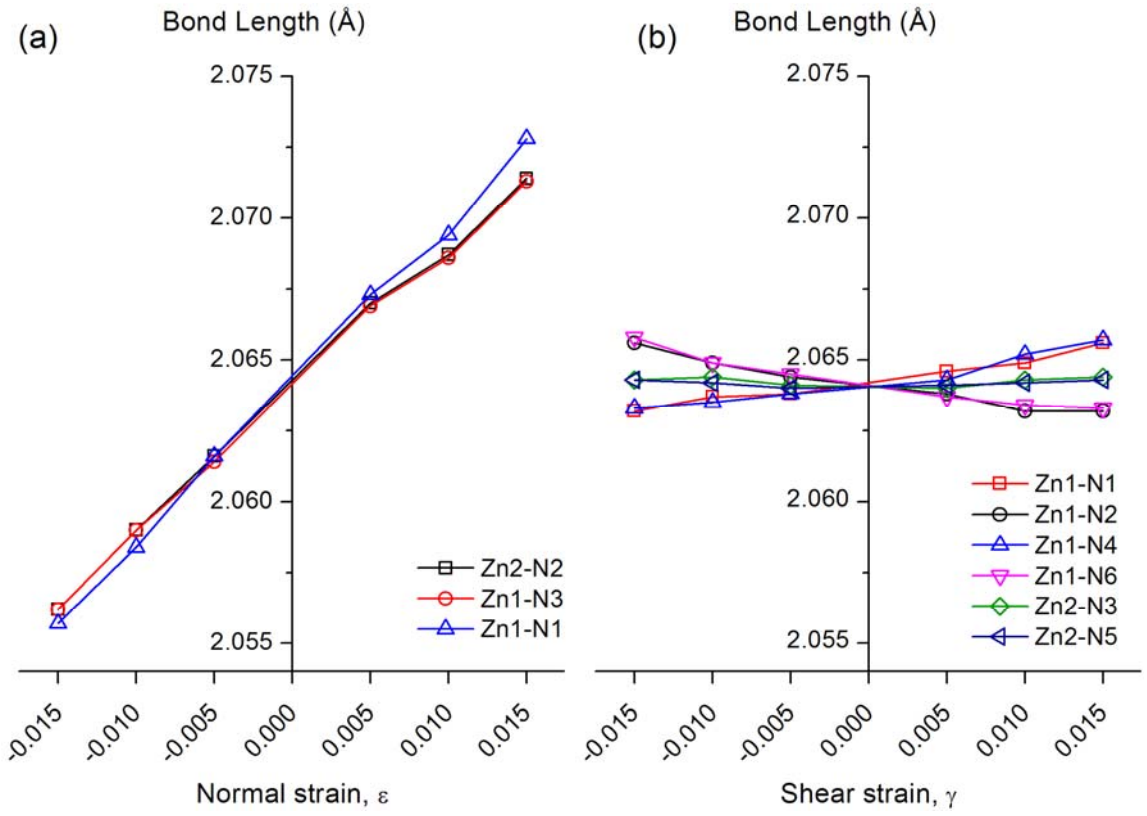

Fig.S5. Variation in the Zn–N bond lengths as a function of applied strain (±1.5%), under a (a) normal/ uniaxial loading, and (b) shear loading. The numerals 1 to 6 refer to the crystallographically independent atomic positions depicted in Fig.S6.

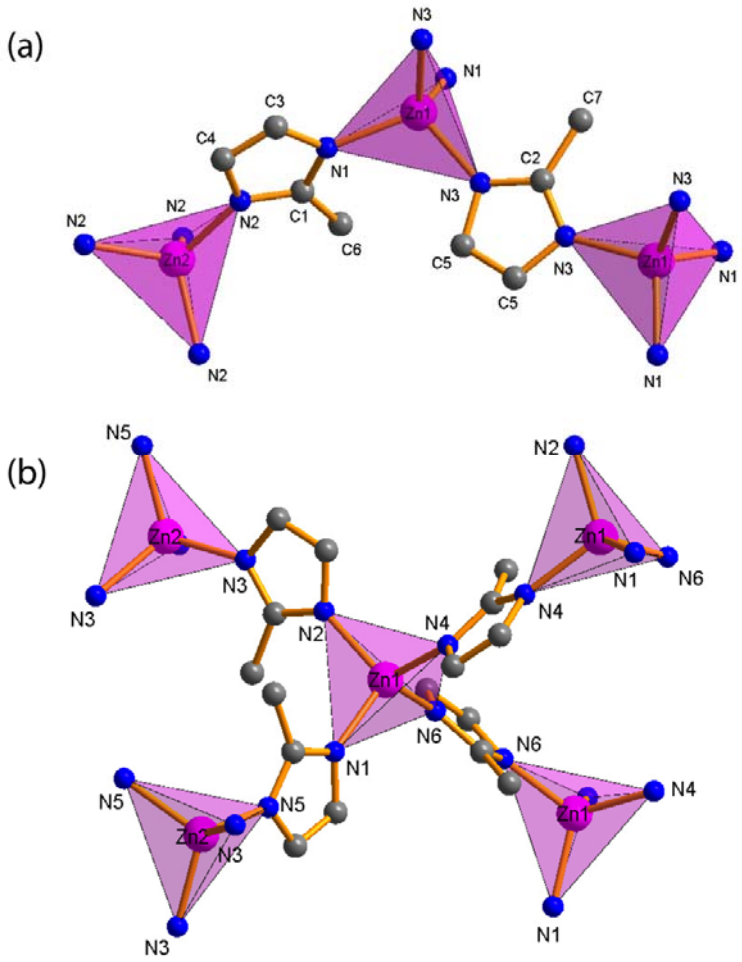

Fig.S6. Ball and stick representation of the asymmetric unit of ZIF-8 under a (a) uniaxial deformation, and (b) shear deformation. The ZnN_4 tetrahedra are in pink. Hydrogen atoms have been omitted for clarity.

Importantly, computed results demonstrate that the exceptionally low shear modulus (*G*) of ZIF-8 is attributed to the *pliant* nature of the ZnN_4 coordination environment. Specifically, for the shear strains being studied here (3% in total), the maximum angular distortion of the tetrahedral N–Zn–N bonds can approach ~3% (*e.g.* N5–Zn2–N3 in Fig.S7(b)). In addition, we note that *bending* of the N–Zn–N bond angles is equally important to facilitate uniaxial strains (*e.g.* ~1% in N3–Zn1–N3 and ~2% in N2–Zn2–N2 angles, see Fig.S7(a)). Furthermore, given that the mIm rings are indeed rigid, computed results reveal that the flexibility of the bridging Zn–mIm–Zn linkages is also attributed to the compliant nature of the ZnN_4 tetrahedra (Fig.S7(c) and (d)). It is interesting to see that the changes in the Zn–mIm–Zn bridging angles are more pronounced under a uniaxial deformation (~1.2%)

than when subjected to a shear deformation (~0.6%; in view of antiparallel shearing). This is because a larger distortion in the bridging angle is *geometrically necessary* to accommodate the imposed uniaxial strains. Of course, the large pore volume in the sodalite cage further facilitates the different modes of elastic strains.

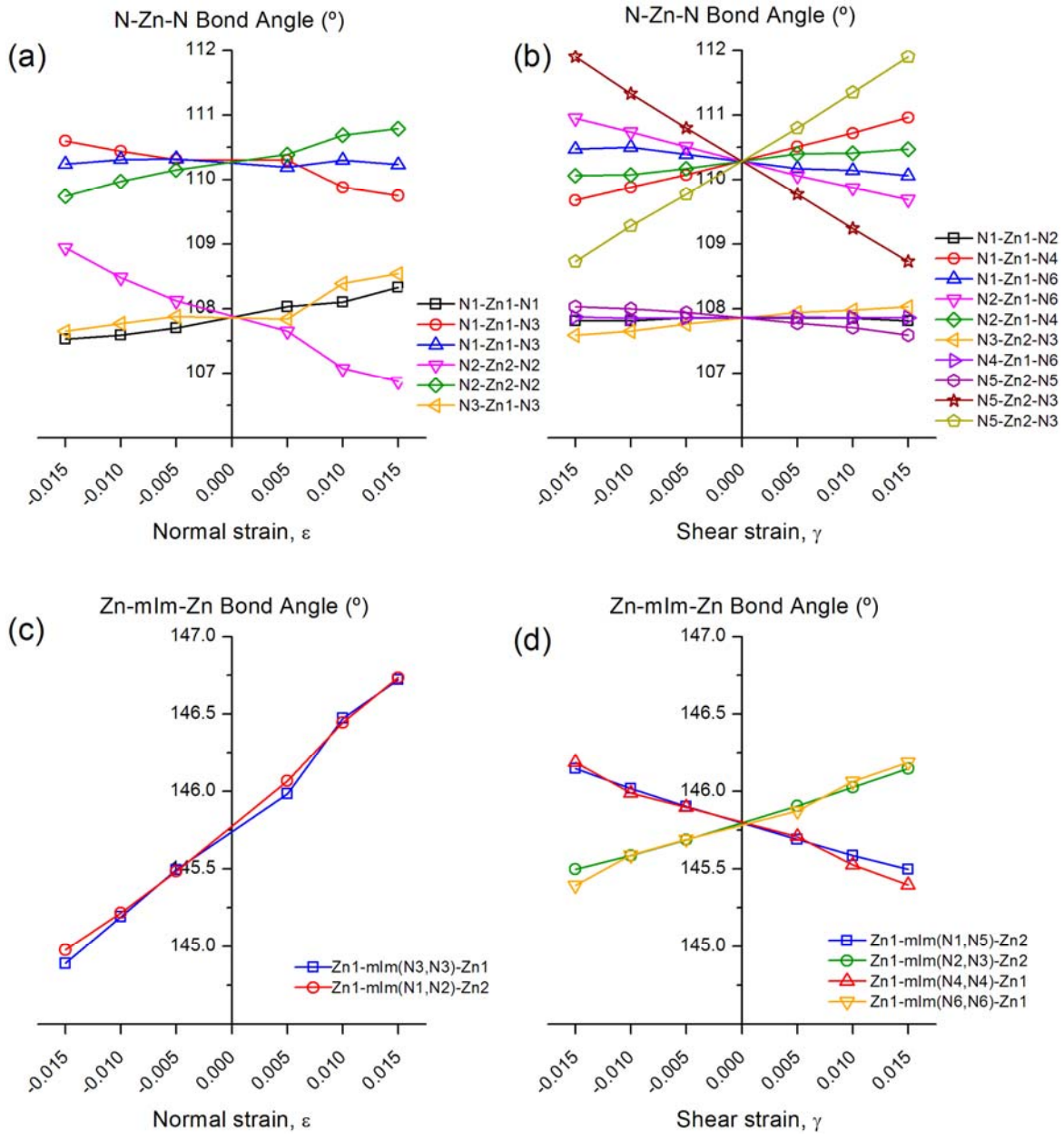

Fig.S7. Variation in the bond angles as a function of applied strain, as associated with the (a) & (b) N–Zn–N tetrahedral angle, and (c) & (d) Zn–mIm–Zn bridging angle. Left column: uniaxial loading; right column: shear loading. The numerals 1 to 6 denote the crystallographically independent atomic positions illustrated in Fig.S6.

We note that variations of the dihedral angles were found to be less relevant, with all changes <1º. Interestingly, our *ab initio* results also reveal large angular variations associated with the rotation of the methyl groups, which is expected given their relatively small energy barrier [14]. However, such rotations only play a minor role in the shear deformation mechanism of ZIF-8 (more details in §3.1).

Additionally, some of us have recently shown that the differential mechanical behaviour of the two isostructural (and dense, *SAV*~10%) ZIFs with the zni topology, $Zn(Im)_2$ and $LiB(Im)_4$, is intrinsically linked to the relative flexibility of the metal coordination polyhedra, that of ZnN_4 versus those of LiN_4 and BN_4. Particularly, the more compliant LiN_4 tetrahedra (visible through the larger N–Li–N bond angles distribution), was identified as responsible for the lower Young's modulus *E* in $LiB(Im)_4$ [16]. On this basis, we now hypothesize that the shear modulus of the lithium boron analogues could be considerably lower than that of their Zn counterparts.

3.3 On the Role of Empirical Dispersion Correction

Recent studies have demonstrated that the inclusion of dispersion interaction corrections can be important in DFT calculations of MOFs. Some of us have shown that such corrections are necessary to capture the bistability of the ultra-flexible aluminium-terephtalate MIL-53 [17], highlighting that dispersion-corrected DFT approaches are required to predict phase transition behaviour and guest-responsive properties of MOF materials. In connection with MOF compressibility, DFT-D calculations have also been successful in predicting the bulk moduli of the $Zn(Im)_2$ and $LiB(Im)_2$ dense analogues [16]. It is apparent from Table S4 and Table S6 that the inclusion of dispersion corrections significantly improves the reproduction of the experimental cell parameters in ZIF-8.

Table S6. Comparison of calculated and experimental unit cell parameters of ZIF-8, obtained using the CP2K and CASTEP DFT codes.

Method	CP2K/ PBE	CP2K/ PBE-D	CP2K/ PBE-D3	CASTEP/ PBE-D	Experimental/ at 3.5 K [14]
a (Å)	17.268	17.029	17.088	16.999	16.990
V (Å^3)	5148.8	4938.4	4989.6	4912.1	4904.3

Hitherto the effects of dispersion corrections on the calculated elastic constants have never been investigated. In this study, we found that the PBE-D and B3LYP-D* dispersion corrections give softer potential energy surfaces (PES) because of the reduction in repulsion between the methyl groups. We can see such an effect by comparing the C_{ij}s (in Table S4) of PBE vs. PBE-D, and in the case of B3LYP vs. B3LYP-D*, particularly with respect to the C_{44} shear coefficient. Given that PBE-D slightly overestimates dispersive interactions, combining PBE-D with a smaller basis set, such as BS1 (has a larger BSSE) leads to a very soft PES, which in turn yields the incorrect set of C_{ij}s.

In contrast, we show that B3LYP-D* gives a more balanced description of weak interactions compared with PBE-D, because of the rescaling of van der Waals radii adopted in its damping function. We also found that the imidazolate anions are better described using a larger basis set, such as the BS2 adopted in this study. In addition, we have attempted a very large basis set, for instance BS3 in combination with PBE-D*, but the results are reminiscent of BS2; the small variations observed can be associated with the variation in terms of the predicted unit cell size (Table S4).

4 Elastic Properties of ZIF-8 Polycrystalline Aggregates

Using the elastic constants C_{ij}s determined from experiments and theory, the elastic properties of the ZIF-8 aggregate can be estimated based on the Voigt, Reuss and Voigt-Reuss-Hill (VRH) averages. Such an isotropic aggregate is representative of a texture-free material, for example, a ZIF-8 powder compact intended for adsorption and storage applications. The Voigt bound defines the upper limit whereas the Reuss bound denotes the lower limit; the VRH bound represents the arithmetic mean of the Voigt and Reuss bounds [15]. Note that for crystals of cubic symmetry, the Reuss and Voigt bounds are indeed identical for treating the bulk modulus and the Poisson's ratio. Previous studies on inorganic cubic crystals [18] reported that the difference between the Voigt and Reuss bounds for the shear modulus (G) increases with elastic anisotropy. Since ZIF-8 is moderately anisotropic (see §7), the difference between the two bounds is relatively small. In this work, we found that *ab initio* calculations based on the B3LYP hybrid functionals are the most consistent with measurements; some of the discrepancies observed here can be attributed to the neglect of thermal effects in the theoretical treatment.

Table S7. Isotropic aggregate elastic properties of ZIF-8

Method	Young's modulus, E (GPa)			Poisson's ratio, ν	Bulk modulus, K (GPa)	Shear modulus, G (GPa)		
	Voigt	Reuss	VRH	Voigt = Reuss = VRH	Voigt = Reuss = VRH	Voigt	Reuss	VRH
Brillouin scattering (295 K)	3.18	3.11	3.145	0.43	7.751	1.11	1.08	1.095
***Ab initio* calculations (0 K):**								
B3LYP (BS2)	3.20	3.10	3.150	0.44	9.23	1.11	1.07	1.091
B3LYP-D*(BS2)	2.78	2.57	2.675	0.45	9.30	0.96	0.89	0.925
PBE (BS2)	2.60	2.54	2.570	0.45	8.71	0.90	0.87	0.885
HF (BS2)	2.88	2.17	2.525	0.45	9.59	0.99	0.74	0.865

5 Nanoindentation Experiments

Nanoindentation studies were performed using an MTS Nanoindenter XP equipped with the dynamic Continuous Stiffness Measurement (CSM) module. Untwinned single crystals with {100}-, {110}- and {111}-oriented facets were first cold-mounted in an epoxy resin (Struers Epofix), followed by incremental grinding (emery paper: up to 4,000 grit) and polishing (diamond suspensions: 6, 3, 1, 0.5, 0.1 μm) to obtain flat surfaces with an RMS roughness of <10 nm (determined from AFM scans). The procedures adopted here have been previously applied successfully for studying a wide range of inorganic-organic (hybrid) framework crystals (*e.g.* [16, 19, 20]).

All measurements were carried out using a three-sided pyramidal Berkovich indenter (end radius ~100 nm), to a maximum surface penetration depth of 500 nm, using a prescribed strain rate of 0.05 s^{-1}. Calibration was performed using a fused silica standard (isotropic), with Young's modulus (E) of 72 GPa and hardness (H) of 9 GPa.

By applying the dynamic CSM mode, the Young's modulus (E) can be obtained as a function of surface penetration depth (h), as shown in Fig.S8. This is achieved by continuously monitoring the change in the elastic contact stiffness (S), which was subsequently converted into the reduced modulus (E_r) [21]:

$$E_r = \frac{\sqrt{\pi}}{2\beta}\frac{S}{\sqrt{A_c}} \qquad (1)$$

where A_c is the contact area established under load (predetermined from a calibrated tip areal function), and β is a constant that depends on the geometry of the indenter (β = 1.034 for a Berkovich tip). The method of Oliver and Pharr [22] was then used to extract the sample Young's modulus (E) from the reduced modulus (E_r):

$$\frac{1}{E_r} = \left(\frac{1-\nu_s^2}{E}\right) + \left(\frac{1-\nu_i^2}{E_i}\right) \qquad (2)$$

where E_i and ν_i are the Young's modulus and Poisson's ratio of the indenter, respectively (for the diamond tip: E_i = 1141 GPa and ν_i = 0.07). In this study, we take the sample Poisson's ratio as ν_s □ 0.4, in line with our Brillouin scattering and *ab initio* results (Table S7). Although it is often noted [22] that the calculated value of E is not particularly sensitive towards the choice of the sample Poisson's ratio (ν_s), here we demonstrate that

for a relatively low-stiffness MOF-type material ($E \lesssim 10$ GPa [23]), such as ZIF-8, this can be significant. As presented in Table S8, ν_s of 0.3 ± 0.1 can result in an up to ≈8% uncertainty in the final value of E; the uncertainty rises to ≈14% when ν_s of 0.2 was adopted instead of applying the averaged value (ν_{VRH}) of about 0.4. As such, for reliable estimation of the elastic modulus of MOFs, knowing their accurate Poisson's ratio can be important. In the absence of experimental data, one may estimate ν from *ab initio* computations, which we have found to be relatively precise for a variety of theoretical methods being considered here (Table S7).

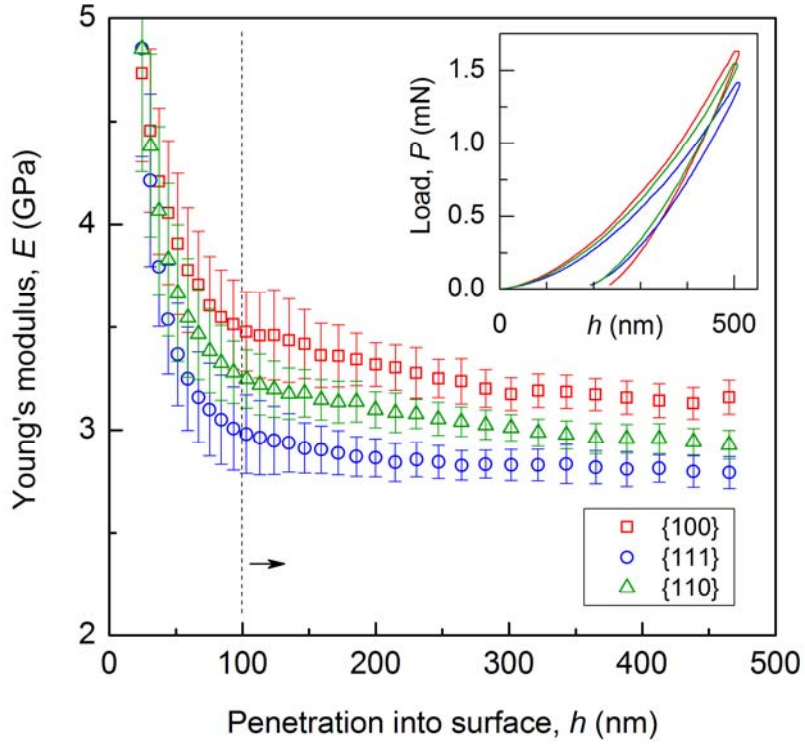

Fig.S8. Single-crystal nanoindentation results of ZIF-8 measured normal to the {100}, {110} and {111} planes, using a Berkovich tip. (Inset) Representative load-displacement (*P*-*h*) curves for a maximum surface penetration depth of 500 nm, which correspond to a maximum load of $P_{max} \approx 1.5$ mN. It can be seen that all the crystal facets experienced significant elastic recovery upon unloading, and the residual depth is ≈200 nm. The Young's moduli (Indentation moduli) appear to be independent of the indenter penetration depth beyond the first 100 nm (consistent with previous study on the ZIF-8's {110} facet [20]), from which we observe that E {100} > E {110} > E {111}. In view of the imperfection of the indenter tip (radius ~100 nm), measurements obtained in the first 100 nm are

deemed unreliable and hence not considered in calculating the average *E* values. The error bars correspond to a standard deviation of at least 10 individual indents.

Table S8. Assessment of the sensitivity of the Young's moduli (indentation moduli) of ZIF-8 determined by the Oliver and Pharr method [22], by assuming different sample Poisson's ratios (ν_s), of which ν_{min} = 0.33; ν_{max} = 0.54; ν_{VRH} = 0.43. The standard deviation of *E* is about $\pm$ 0.1 GPa.

Poisson's ratio, ν_s	Young's modulus/ Indentation modulus (GPa)		
	E {100}	*E* {110}	*E* {111}
0.2	3.76	3.52	3.28
0.3	3.57	3.33	3.11
0.4	3.29	3.07	2.87
0.5	2.94	2.75	2.56

Furthermore, we note that the application of nanoindentation to anisotropic materials requires additional scrutiny because of the following known limitations, among them are:

- The Oliver and Pharr method [22], *i.e.* Eqn.(2), was derived on the assumption that the material being probed is *homogeneous* and *elastically isotropic* in nature. Clearly, this is **not** the case even for most single crystals with cubic symmetry [15]. Such a deviation in relation to cubic crystals has been carefully studied by Vlassak and Nix [24], who proposed corrections that have been demonstrated to work well for certain classes of metallic systems. In another study on hexagonal single crystals, Hay *et al.* [25] reported that for β-silicon nitride, the Young's modulus is underestimated by about 20% in the stiffest direction, whereas in the most compliant direction, it is overestimated by about 10%.
- Given that the Berkovich indenter tip is a three-dimensional pyramidal object, the nature of the stress field developed under the indenter is **not** truly unidirectional [21], such that the "Young's moduli" measured this way may deviate from the intrinsic values, but biased towards the modulus in the direction of testing. For this reason, it is more appropriate to term the elastic modulus determined *via* nanoindentation as the "Indentation Modulus" instead; the current consensus is that

the modulus obtained by this way represents an average of the single-crystal anisotropic elastic constants.

Despite the aforementioned shortcomings, in this study of ZIF-8, we found that nanoindentation can accurately determine the Young's moduli for both the {110} and {111} facets, but the modulus of the stiffest direction, E {100}, was underestimated by approximately 13% (when ν_s □ 0.4, see Table S8); this is reminiscent to the findings of Hay *et al.* [25]. It appears therefore, that despite its known shortcomings, nanoindentation provides an excellent first-order estimate of the intrinsic Young's modulus for MOF single crystals that are *moderately anisotropic*, for which we propose Zener ratios in the range $0.7 \leq A \leq 1.3$ (isotropic $A = 1$). Nevertheless, correcting for the uncertainties associated with nanoindentation of highly anisotropic single crystals warrants future investigations.

6 Crystal Structure of ZIF-8 *vs.* Zeolite Sodalite

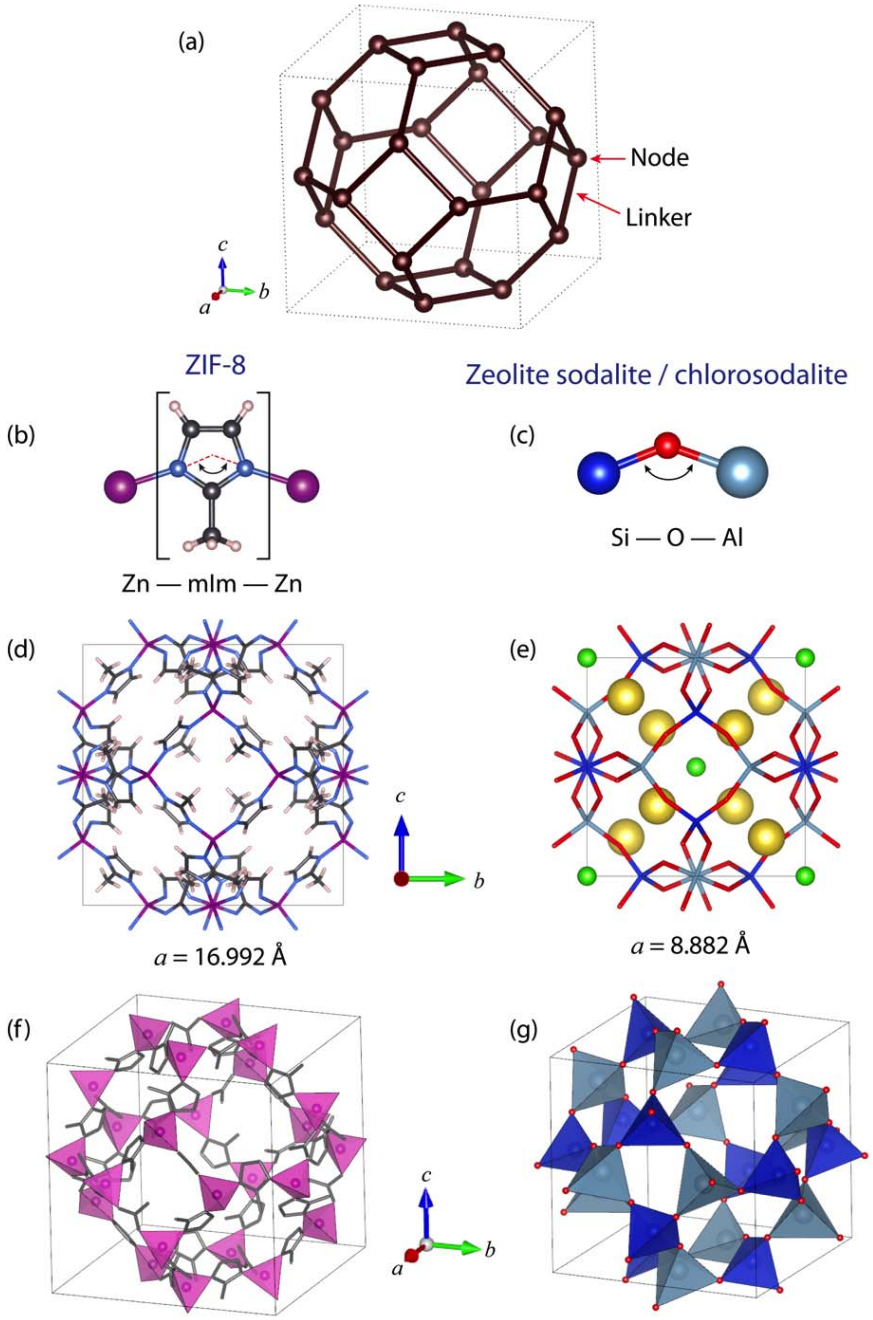

Fig.S9. (a) A cubo-octahedral sodalite (SOD) cage depicting the 4- and 6-membered rings oriented normal to the $\langle 100 \rangle$ and $\langle 111 \rangle$ axes, respectively. (b) & (c) Zn–mIm–Zn and Si–O–Al linkages found in ZIF-8 and chlorosodalite, respectively. Notably, the organic linkers in ZIFs (*e.g.* 2-methylimidazolate in ZIF-8) play the role of oxygen in conventional zeolites, giving rise to bridging linkages that subtend an angle of ~145º at the Im ring

center. (d) & (e) Stick representations comparing the open-framework structure of ZIF-8 to that of chlorosodalite, both viewed down the *a*-axis; note that the Na^+ and Cl^- ions occupy the accessible porosity in the latter. (f) Polyhedral representation of ZIF-8, in which the ZnN_4 coordination environment is represented by the pink tetrahedron. Hydrogen atoms have been omitted for clarity. (g) Polyhedral representation of chlorosodalite, in which the dark blue and turquoise tetrahedra are SiO_4 and AlO_4, respectively. Here the Na^+ and Cl^- ions have been omitted for clarity. [Pink: zinc; blue: nitrogen; grey: carbon; white: hydrogen; dark blue: silicon; red: oxygen; turquoise: aluminium; yellow: sodium; green: chlorine]

As shown in Fig.S9, the topology of cubic ZIF-8, [$Zn(mIm)_2$; mIm = 2-methylimidazolate] is identical to that of zeolite sodalite (*chlorosodalite* [$Na_4Al_3Si_3O_{12}Cl$] [26]), the latter is a naturally occurring mineral with an aluminosilicate framework. While chlorosodalite has a purely inorganic framework architecture comprising Si–O–Al linkages, ZIF-8 features Zn–mIm–Zn connectivities, for which the bridging coordination motif of the imidazolate ions yields a more extended open-framework featuring an appreciably larger unit cell. Extensive studies (*e.g.* [27-31]) have established that the flexibility of inorganic zeolites is dominated by the bending of Si–O–Al angles connecting the rigid SiO_4 and AlO_4 tetrahedra (or, the corresponding Si–O–Si angles in siliceous zeolites, *e.g.* [32, 33]). The elastic properties of chlorosodalite are summarized in §8 (see Table S9).

7 Elasticity of MOF-5 *vs.* ZIF-8

Since 2006, the single-crystal elastic constants C_{ij}s of MOF-5 [$ZnO_4(BDC)_3$; BDC = 1,4-benzenedicarboxylate [34]] have been extensively studied through a range of computational techniques. However, the reported values show inconsistencies and appear to be somewhat sensitive to the different approaches being adopted [23]. For example, MOF-5's C_{11} was predicted to be 44.53 GPa (10 K) *via* the MD method [35], but DFT (GGA) calculations obtained a considerably lower value of 28.5 GPa (0 K) [36]. Likewise, its C_{44} shear coefficient ranges from 1.16 GPa [37] to 3.6 GPa [36] (excluding an outlier at 7.54 GPa [38]). Direct measurements of the elastic constants of MOF-5, however, have yet to be reported. This might be related to the fact that MOF-5 exhibits very poor hydrothermal stability and decomposes rapidly in humid conditions (especially upon removal from the mother liquor, leading to structural collapse [39]). Nevertheless, interesting insights can be gained based on the computed elastic constants [23]. The solvent accessible volume (*SAV*) in MOF-5 is ~80%, which is significantly larger than that of ZIF-8 (*SAV*~50%), as depicted in Fig.S10. The calculated framework density (determined from the X-ray structure) of the evacuated MOF-5 is ~0.59 g/cm^3 (*vs.* ~0.95 g/cm^3 in ZIF-8).

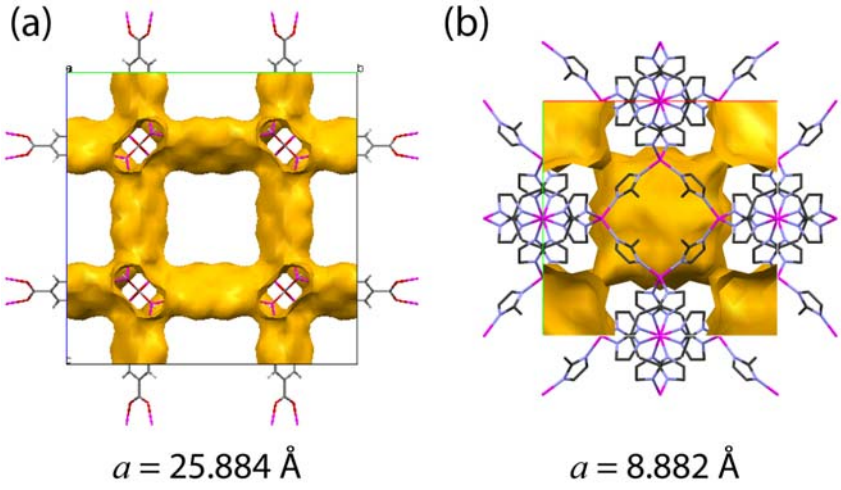

Fig.S10. Pore morphologies and solvent accessible volume (*SAV*) in (a) MOF-5 and (b) ZIF-8. The yellow surfaces designate the outer boundaries of the nano-sized pores. It can be seen that the MOF-8 framework is considerably more expanded, featuring interconnected neighbouring pores linking the adjacent unit cells (along the cube axes).

Conversely, ZIF-8 consists of a large central pore connected by 8 relatively narrow channels to the adjacent unit cells. [Pink: zinc, grey: carbon, blue: nitrogen; red: oxygen]

For comparison with the elasticity of ZIF-8, in what follows, we present the representation surface plots corresponding to the acoustic velocity (*V*), Young's modulus (*E*), shear modulus (*G*) and Poisson's ratio (ν) of MOF-5, as derived from the elastic constants calculated by Bahr *et al.* [36] using the density-functional theory (GGA, 0 K): C_{11} = 28.5 GPa, C_{12} = 12.1 GPa and C_{44} = 1.7 GPa. Importantly, the elastic constants of MOF-5 as computed at the same level of theory adopted in the present work (*i.e.* B3LYP(BS2): C_{11} = 28.3 GPa, C_{12} = 11.1 GPa and C_{44} = 1.1 GPa) are in excellent agreement with the values reported by Bahr *et. al* [36]. Particularly, although the shear coefficient C_{44} (= G_{min}) predicted for MOF-5 is relatively small, we note that the C_{44} directly measured in this study for ZIF-8 is even lower (C_{44} < 1 GPa).

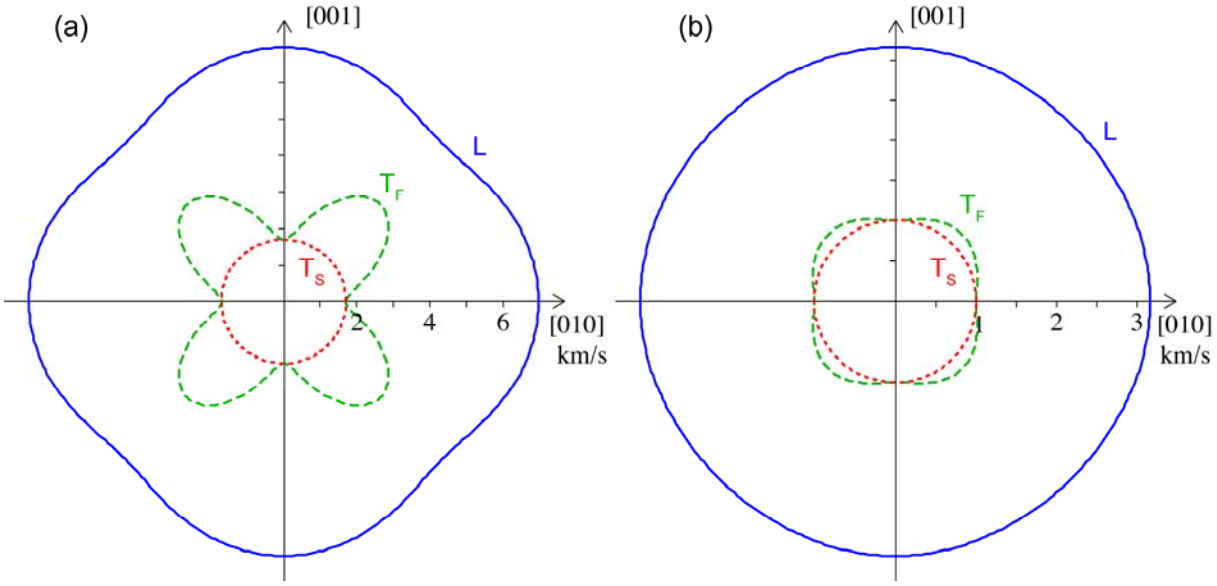

Fig.S11. Acoustic wave velocities (*V*) down the [100] cube axis, calculated from the elastic constants of (a) MOF-5 (C_{ij}s from DFT [36]) vs. (b) ZIF-8 (experimental C_{ij}s in Table S3). Notice the different scales between the two plots. The anisotropy in MOF-5 is more pronounced, with longitudinal wave velocities, L_{max} & L_{min} of 6.95 and 5.80 km s^{-1}, respectively; its maximum and minimum transverse waves (T_{max} & T_{min}) are 3.73 and 1.70 km s^{-1}, respectively. In contrast, ZIF-8 appears to be moderately anisotropic, with L_{max} of just 3.17 km s^{-1}, while the T_{max} & T_{min} are 1.18 and 1.01 km s^{-1}, respectively. (Tensorial analyses were performed using the *ElAM* program [40])

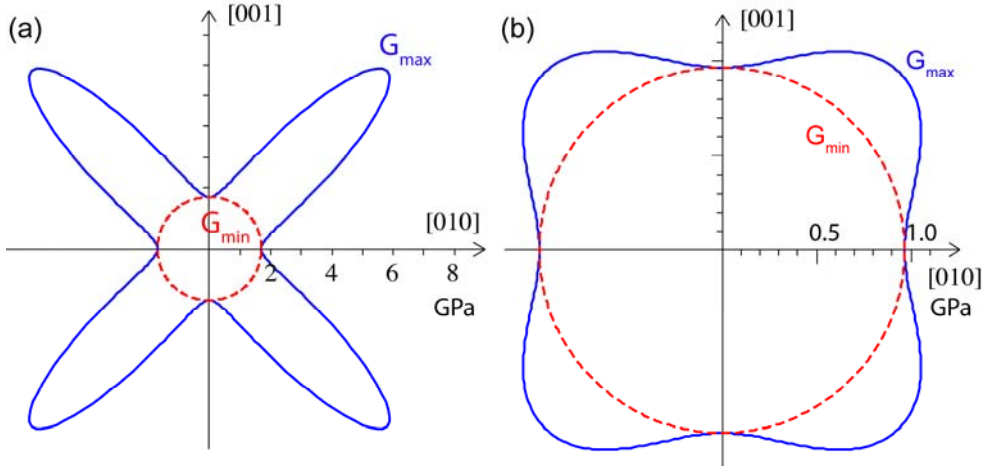

Fig.S12. Shear modulus (G) of (a) MOF-5 vs. (b) ZIF-8 down the [100] axis, showing both the maximum and minimum representation surfaces. In MOF-5, the G_{max} is 4.3 GPa along the $\langle 110 \rangle$ axes, while G_{min} is 1.7 GPa along the $\langle 100 \rangle$ cube axes. In ZIF-8, although the maximum and minimum shear moduli exist in the same orientations as in MOF-5, the degree of anisotropy of the former is less pronounced, with G_{max} and G_{min} of 1.33 and 0.97 GPa, respectively. Notably, the maximum shear modulus in ZIF-8 is only about one third of that predicted for MOF-5.

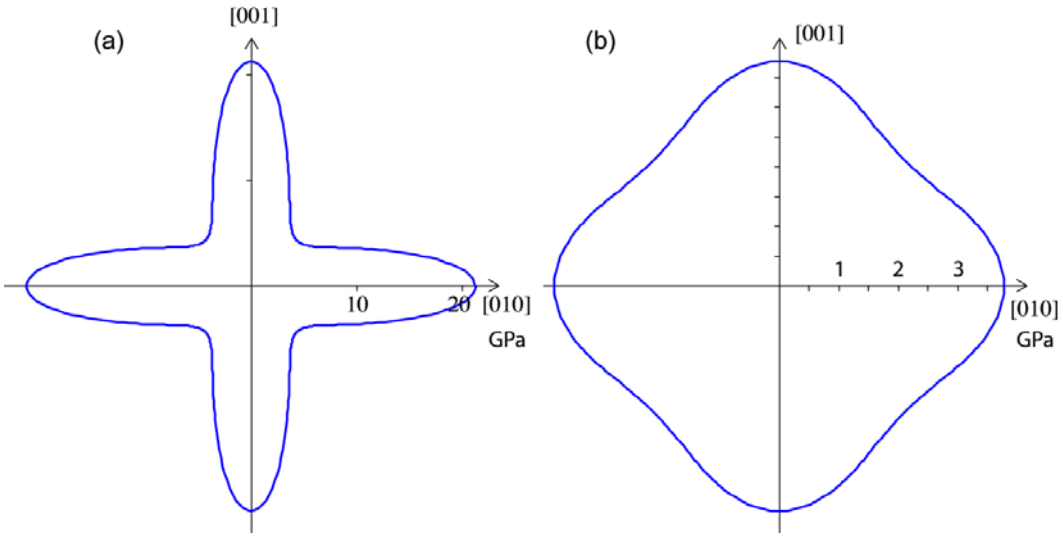

Fig.S13. Young's modulus (E) of (a) MOF-5 vs. (b) ZIF-8 down the [100] direction. In MOF-5, E_{max} and E_{min} are 21.3 GPa and 4.9 GPa respectively, from which we found E_{max}/E_{min} = 4.35. The MOF-5 framework is therefore the stiffest along the $\langle 100 \rangle$ cube axes, which directly correspond to the orientations of the rigid BDC linkers; the structure is

the most compliant along the $\langle 111 \rangle$ cube diagonals. The maximum and minimum Young's moduli of ZIF-8 are of a similar fashion to that of MOF-5, but its maximum stiffness is an order of magnitude lower (E_{max} and E_{min} of 3.77 GPa and 2.78 GPa respectively; E_{max}/E_{min} = 1.35).

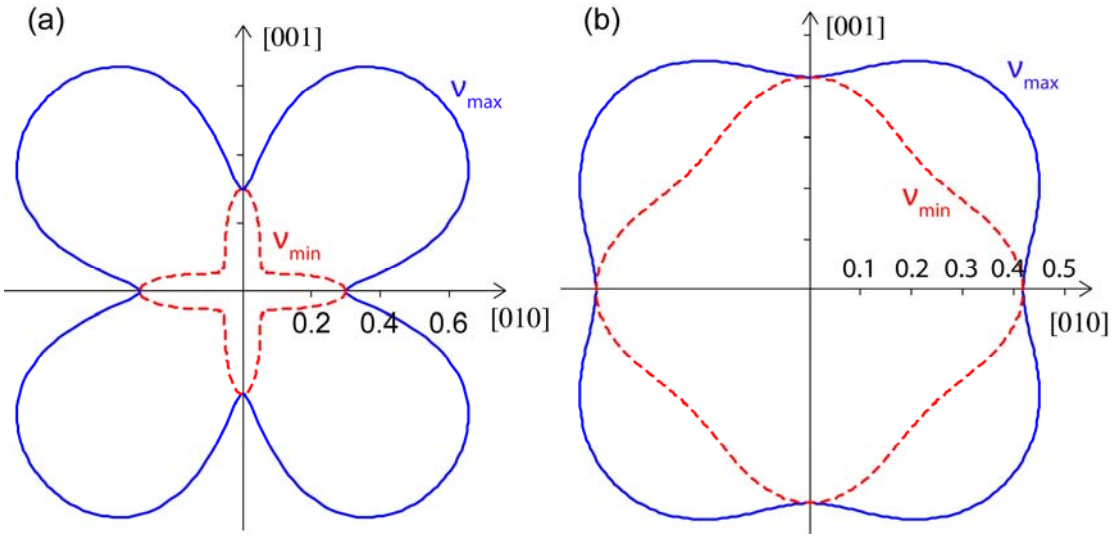

Fig.S14. Poisson's ratio (ν) of (a) MOF-5 vs. (b) ZIF-8, highlighting the differences between their maximum and minimum representation surfaces. For both structures, ν_{max} corresponds to $\nu\langle 110, 1\bar{1}0 \rangle$whereas ν_{min} corresponds to $\nu\langle 110, 001 \rangle$. In MOF-5, ν_{max} and ν_{min} are 0.80 and 0.09, respectively; in ZIF-8, they are 0.54 and 0.33, respectively. Again, the Poisson's ratio in MOF-5 is highly anisotropic when compared to that of ZIF-8.

8 Elasticity of Inorganic Framework Materials

Table S9. Elastic properties of 3-D inorganic frameworks derived from single-crystal elastic constants C_{ij}s. These open-framework structures are made of corner-sharing AlO_4 and/or SiO_4 tetrahedra (T), and are known to be relatively "soft" (pliant) and compressible due to bending of their T–O–T angles [27-30, 32, 41].

Inorganic Open-Framework Structure	**Method**	**Ref**	**Calc. Density g/cm^3**	**Elastic Constants, C_{ij}s, GPa**	**Acoustic Velocities, *V*, km/s L(*Max, Min*) T(*Max, Min*)**	**Shear Modulus, *G*, GPa (*Max,Min*);*VRH***	**Young's Modulus, *E*, GPa (*Max,Min*);*VRH***	**Poisson's Ratio, *ν** (*Max,Min*);*VRH***	**Bulk Modulus K_{VRH}, GPa**
Chlorosodalite [SOD, cubic, *A* = 1.46 based on [30]]	Ultrasonic measurement	[30]	2.31	C_{11} = 88.52(71) C_{12} = 38.70(50) C_{44} = 36.46(33)	L(6.71, 6.19) T(3.97, 3.28)	(36.46, 24.91); 31.30	(89.67, 64.98); 78.99	(0.38, 0.12); 0.265	55.31
	Force-field molecular modelling	[42]		C_{11} = 144.9 C_{12} = 38.58 C_{44} = 39.27	L(7.92, 7.40) T(4.80, 4.12)	(53.16, 39.27); 44.34	(128.68, 100.11); 110.89	(0.35, 0.17); 0.25	74.02
	Diamond anvil cell (DAC)	[27]		—	—	—	—	—	52(8)
Analcime [ANA, cubic, *A* = 0.71]	Brillouin scattering	[29]	2.249	C_{11} = 112.5(1.1) C_{12} = 33.4(4) C_{44} = 27.9(3)	L(7.07, 6.57) T(4.19, 3.52)	(39.55, 27.90); 32.10	(97.21, 72.43); 81.66	(0.39, 0.18); 0.275	59.77
Natrolite [NAT, orthorhombic]	Brillouin scattering	[29]	2.239	C_{11} = 70.4(7) C_{22} = 72.0(7) C_{33} = 132.3(1.2) C_{44} = 26.8(4) C_{55} = 26.5(4) C_{66} = 51.3(6) C_{12} = 26.0(6) C_{13} = 32.8(9) C_{23} = 31.8(9)	L(7.69, 5.61) T(4.79, 3.18)	(51.30, 22.59); 31.56	(110.81, 57.17); 77.81	(0.46, –0.12); 0.24	48.49

Pollucite [NAT, cubic, A = 0.68]	Brillouin scattering	[43]	2.930	C_{11} = 105.0(1.3) C_{12} = 25.7(6) C_{44} = 27.0(3)	L(5.99, 5.48) T(3.68, 3.04)	(39.65, 27.00); 31.5	(94.89, 69.08); 78.6	(0.37, 0.15); 0.245	52.2
MFI silicalite [MFI, orthorhombic]	Brillouin scattering	[32]	2.045	C_{11} = 84.5(8) C_{22} = 68.2(1.2) C_{33} = 79.0(8) C_{44} = 22.6(2) C_{55} = 23.5(4) C_{66} = 21.2(2) C_{12} = –1.52(2) C_{13} = 19.9(2) C_{23} = 10.3(3)	L(6.43, 5.31) T(4.34, 3.22)	(38.34, 21.20); 26.29	(79.23, 52.21); 61.77	(0.36, –0.06); 0.18	31.65
α-Cristobalite [SiO_2, tetragonal]	Brillouin scattering	[44]	2.318	C_{11} = 59.4(5) C_{33} = 42.4(7) C_{44} = 67.2(4) C_{66} = 25.7(4) C_{12} = 3.8(8) C_{13} = –4.4(9)	L(6.26, 3.89) T(5.72, 3.33)	(67.20, 25.70); 39.06	(70.10, 41.79); 65.18	(0.10, –0.51); –0.15	16.37
Clathrasil (Dodecasil 3C) [SiO_2, cubic A = 1.09]	Brillouin scattering	[45]	2.0	C_{11} = 55.2(0.6) C_{12} = 11.1(0.7) C_{44} = 24.1(0.5)	L(5.38, 5.25) T(3.47, 3.32)	(24.10, 22.05); 23.26	(55.13, 51.48); 53.65	(0.18, 0.12); 0.15	25.8

*A negative Poisson's (NPR) signifies an *auxetic* behaviour.

VRH = Voigt-Reuss-Hill averages

9 Example of input file for CRYSTAL09: ZIF-8, B3LYP (BS2)

```
CRYSTAL
0 0 0
 217
17.34813274
8
 6    -1.239805747828E-01 -4.889707501755E-01  1.239805747828E-01
 6    -1.283379401818E-01  4.010585347062E-01  1.840201114945E-01
 6    -9.770358085485E-02 -4.110799484781E-01  9.770358085485E-02
 7    -9.040898839273E-02  4.709793541986E-01  1.814597975546E-01
30     5.441378642834E-17  5.000000000000E-01  2.500000000000E-01
 1    -1.125088450556E-01  3.567954015273E-01  2.246396383342E-01
 1    -5.323605237233E-02 -4.160180622849E-01  5.323605237233E-02
 1    -1.453674898532E-01 -3.781433287150E-01  7.328185655768E-02
ELASTCON
STEPSIZE
0.005
PRINT
TOLDEG
0.0002
TOLDEX
0.0004
END
ENDG
6 5
0 0 6 2.0 1.00
  0.4563240000D+04  0.1966650000D-02
  0.6820240000D+03  0.1523060000D-01
  0.1549730000D+03  0.7612690000D-01
  0.4445530000D+02  0.2608010000D+00
  0.1302900000D+02  0.6164620000D+00
  0.1827730000D+01  0.2210060000D+00
0 1 3 4.0 1.00
  0.2096420000D+02  0.1146600000D+00  0.4024870000D-01
  0.4803310000D+01  0.9199990000D+00  0.2375940000D+00
  0.1459330000D+01 -0.3030680000D-02  0.8158540000D+00
0 1 1 0.0 1.00
  0.4834560000D+00  0.1000000000D+01  0.1000000000D+01
0 1 1 0.0 1.00
  0.1455850000D+00  0.1000000000D+01  0.1000000000D+01
0 3 1 0.0 1.00
  0.6260000000D+00  0.1000000000D+01
7 5
0 0 6 2.0 1.00
  0.6293480000D+04  0.1969790000D-02
  0.9490440000D+03  0.1496130000D-01
  0.2187760000D+03  0.7350060000D-01
  0.6369160000D+02  0.2489370000D+00
  0.1882820000D+02  0.6024600000D+00
  0.2720230000D+01  0.2562020000D+00
0 1 3 5.0 1.00
  0.3063310000D+02  0.1119060000D+00  0.3831190000D-01
  0.7026140000D+01  0.9216660000D+00  0.2374030000D+00
  0.2112050000D+01 -0.2569190000D-02  0.8175920000D+00
0 1 1 0.0 1.00
  0.6840090000D+00  0.1000000000D+01  0.1000000000D+01
0 1 1 0.0 1.00
  0.2008780000D+00  0.1000000000D+01  0.1000000000D+01
0 3 1 0.0 1.00
  0.9130000000D+00  0.1000000000D+01
1 4
0 0 3 1.0 1.00
  0.3386500000D+02  0.2549380000D-01
  0.5094790000D+01  0.1903730000D+00
  0.1158790000D+01  0.8521610000D+00
0 0 1 0.0 1.00
```

```
  0.3258400000D+00  0.1000000000D+01
0 0 1 0.0 1.00
  0.1027410000D+00  0.1000000000D+01
0 2 1 0.0 1.00
  0.7500000000D+00  0.1000000000D+01
30 9
0 0 8 2.0 1.0
417016.5    0.00023
60504.2    0.00192
12907.9    0.01101
3375.74   0.04978
1018.11   0.16918
352.55   0.36771
138.19   0.40244
57.851  0.14386
0 1 6 8.0 1.0
1079.2   -0.00620   0.00889
256.52  -0.07029   0.06384
85.999 -0.13721   0.22039
34.318  0.26987   0.40560
14.348  0.59918   0.41370
4.7769 0.32239   0.34974
0 1 4 8.0 1.0
60.891  0.00679  -0.00895
25.082 -0.08468  -0.03333
10.620 -0.34709   0.08119
4.3076 0.40633   0.56518
0 1 1 2.0 1.0
1.748  1.0 1.0
0 1 1 0.0 1.0
0.700 1.0 1.0
0 1 1 0.0 1.0
0.179 1.0 1.0
0 3 4 10.0 1.0
57.345   0.02857
16.082   0.15686
5.3493  0.38663
1.7548  0.47766
0 3 1 0.0 1.0
0.535 1.0
0 4 1 0.0 1.0
0.800 1.00
99 0
ENDB
DFT
B3LYP
XLGRID
END
SCFDIR
BIPOSIZE
10000000
EXCHSIZE
20000000
SHRINK
2 2
TOLINTEG
7 7 7 7 16
FMIXING
30
LEVSHIFT
6 1
TOLDEE
8
ENDSCF
```

10 References

[1] K. S. Park*, et al.*, Proc. Natl. Acad. Sci. USA **103**, 10186 (2006).

[2] C. H. Whitfield*, et al.*, Rev. Sci. Instrum. **47**, 942 (1976).

[3] D. J. Weidner and H. R. Carleton, J. Geophys. Res. **82**, 1334 (1977).

[4] C. C. Chen*, et al.*, Am. Miner. **86**, 1525 (2001); C. C. Lin and C. C. Chen, Eur. J. Mineral. **23**, 35 (2011); L. G. Liu*, et al.*, Phys. Chem. Miner. **32**, 97 (2005); L. G. Liu*, et al.*, Solid State Commun. **132**, 517 (2004).

[5] P. F. Chen*, et al.*, Phys. Earth Planet. Inter. **155**, 73 (2006).

[6] R. Dovesi*, et al.*, Z. Kristall. **220**, 571 (2005); R. Dovesi*, et al.*, (2009).

[7] B. Civalleri*, et al.*, CrystEngComm **8**, 364 (2006).

[8] W. F. Perger*, et al.*, Comput. Phys. Commun. **180**, 1753 (2009).

[9] A. D. Becke, J. Chem. Phys. **98**, 5648 (1993); C. T. Lee*, et al.*, Phys. Rev. B **37**, 785 (1988).

[10] J. P. Perdew*, et al.*, Phys. Rev. Lett. **77**, 3865 (1996).

[11] B. Civalleri*, et al.*, CrystEngComm **10**, 405 (2008).

[12] S. Grimme, J. Comput. Chem. **27**, 1787 (2006).

[13] S. A. Moggach*, et al.*, Angew. Chem. Int. Ed. **48**, 7087 (2009).

[14] W. Zhou*, et al.*, J. Phys. Chem. A **112**, 12602 (2008).

[15] J. F. Nye, *Physical Properties of Crystals* (Clarendon Press, Oxford, 1985).

[16] T. D. Bennett*, et al.*, Chem. Eur. J. **16**, 10684 (2010).

[17] A. M. Walker*, et al.*, Angew. Chem. Int. Ed. **49**, 7501 (2010).

[18] D. H. Chung and W. R. Buessem, J. Appl. Phys. **38**, 2535 (1967); R. J. Angel*, et al.*, Eur. J. Mineral. **21**, 525 (2009).

[19] T. D. Bennett*, et al.*, Phys. Rev. Lett. **104**, 115503 (2010); M. Kosa*, et al.*, ChemPhysChem **11**, 2332 (2010); J. C. Tan*, et al.*, J. Am. Chem. Soc. **131**, 14252 (2009); J. C. Tan*, et al.*, Acta. Mater. **57**, 3481 (2009).

[20] J. C. Tan*, et al.*, Proc. Natl. Acad. Sci. USA **107**, 9938 (2010).

[21] A. C. Fisher-Cripps, *Nanoindentation* (Springer, New York, 2004).

[22] W. C. Oliver and G. M. Pharr, J. Mater. Res. **7**, 1564 (1992); W. C. Oliver and G. M. Pharr, J. Mater. Res. **19**, 3 (2004).

[23] J. C. Tan and A. K. Cheetham, Chem. Soc. Rev. **40**, 1059 (2011).

[24] J. J. Vlassak and W. D. Nix, Philos. Mag. A **67**, 1045 (1993); J. J. Vlassak and W. D. Nix, J. Mech. Phys. Solids **42**, 1223 (1994).

[25] J. C. Hay*, et al.*, J. Am. Ceram. Soc. **81**, 2661 (1998).

[26] R. K. McMullan*, et al.*, Acta Crystallogr. Sect. B-Struct. Sci. **52**, 616 (1996); L. Pauling, Z. Kristall. **74**, 213 (1930).

[27] R. M. Hazen and Z. D. Sharp, Am. Miner. **73**, 1120 (1988).

[28] Y. M. Huang, J. Mater. Chem. **8**, 1067 (1998).

[29] C. Sanchez-Valle*, et al.*, J. Appl. Phys. **98** (2005).

[30] Z. Li*, et al.*, Appl. Phys. Lett. **55**, 1730 (1989).

[31] G. D. Gatta, Eur. J. Mineral. **17**, 411 (2005).

[32] C. Sanchez-Valle*, et al.*, J. Chem. Phys. **128** (2008).

[33] A. Sartbaeva*, et al.*, Nat. Mater. **5**, 962 (2006).

[34] H. Li*, et al.*, Nature **402**, 276 (1999).

[35] S. S. Han and W. A. Goddard, J. Phys. Chem. C **111**, 15185 (2007).

[36] D. F. Bahr*, et al.*, Phys. Rev. B **76**, 184106 (2007).

[37] W. Zhou and T. Yildirim, Phys. Rev. B **74**, 180301 (2006).

[38] M. Mattesini*, et al.*, Phys. Rev. B **73**, 094111 (2006).

[39] S. S. Kaye*, et al.*, J. Am. Chem. Soc. **129**, 14176 (2007); J. J. Low*, et al.*, J. Am. Chem. Soc. **131**, 15834 (2009).

[40] A. Marmier*, et al.*, Comput. Phys. Commun. **181**, 2102 (2010).

[41] J. N. Grima*, et al.*, Phys. Status Solidi B **244**, 866 (2007); J. N. Grima*, et al.*, Adv. Mater. **12**, 1912 (2000).

[42] J. J. Williams*, et al.*, Appl. Phys. Lett. **88** (2006).

[43] C. Sanchez-Valle*, et al.*, J. Appl. Phys. **108** (2010).

[44] A. Yeganeh-Haeri*, et al.*, Science **257**, 650 (1992).

[45] R. Freimann and H. Kuppers, Phys Status Solidi A **123**, K123 (1991).